Experiments in Fluids 34 (2003) 291–303
DOI 10.1007/s00348-002-0559-8

Quantitative studies of the wakes of freely flying birds in a low-turbulence wind tunnel

G.R. Spedding, A. Hedenström, M. Rosén

Abstract A novel application of DPIV methods is presented for measuring velocity and vorticity distributions in vertical cross sections through the wake of a freely flying bird (thrush nightingale) in a wind tunnel. A dual-camera system is used, and successive cross-correlation operations remove lens/camera distortions, and then the undisturbed background flow, so that the final operation simply examines the disturbance effect of the bird alone. The concentration and tuning of processing methods to the disturbance quantities allows full exploitation of the correlation calculation and estimation algorithms. Since the ultimate objective is to deduce forces and power requirements on the bird itself from the wake structure, the analytical procedure is followed through an example on a fixed airfoil, before sample results from extensive bird flight tests are described. The wake structure of the thrush nightingale in slow (5-m/s) flight is qualitatively quite similar to those previously described in the literature, but certain quantitative details are different in important respects.

1 Introduction

1.1 Flight models and vortex wakes

The aerodynamics of animal flight, particularly that of birds, has long held a strong fascination for the earth-bound human. Reviews of scientific aspects can be found in Lighthill (1975), Norberg (1990) and Spedding (1992). The basic aerodynamic mechanisms are quite well understood, yet many details remain largely a matter of conjecture, as the significance of the unsteady motion of lifting surfaces with complicated geometry and kinematics (passive flexure, porosity) is frequently far from clear. Most analytical work requires restrictive assumptions either on flapping amplitude, or presence or absence of viscous effects (such as boundary layer separation), or on the comparative importance of unsteady terms, usually measured by the magnitude of a reduced frequency

$$k = \frac{2\pi fc}{U}, \tag{1}$$

where f is the flapping frequency, c is a reference chord length and U is a mean flow speed. Typical numbers for bird flight might involve U=10 m/s, f=10 Hz and c=10 cm, so $k \simeq 0.6$. Analytic or numerical prediction of accurate surface pressure distributions under these circumstances is not feasible. However, as for any object immersed in a fluid, momentum and energy conservation laws dictate that the action of the surrounding air on the wings and body giving rise to the forces experienced by the bird be accompanied by equal and opposite reaction forces manifested as disturbances in the fluid that can be observed in the wake. The net rate of increase or decrease in wake momentum corresponds exactly to the net force exerted on the animal. Since the aerodynamic power requirement can, in principle, be calculated from the rate of increase of wake kinetic energy, which can be related to the momentum increase, the most successful and/or practical theoretical models of bird flight (e.g. Pennycuick 1975, 1989; Rayner 1979a, 1979b) do not concern themselves with the wing motions at all, but rather model the wake structure itself.

The high-amplitude, time-varying wing motions, together with the interesting Reynolds number range (for the 'standard bird' example given above):

$$Re = \frac{Uc}{\nu} \simeq 6.7 \times 10^4,$$

where ν is the kinematic viscosity, seem to guarantee that the wake structure will not be simple. Partly as a consequence, there have been only four previous quantitative studies of the wake structure behind flying birds: for a pigeon and jackdaw in slow flight (Spedding et al. 1984; Spedding 1986), and for a kestrel in gliding and medium-speed (cruising) flight (Spedding 1987a, 1987b).

1.2 Measurement techniques

In previous studies, the wake analysis was technically demanding, involving three-dimensional tracking of many

Received: 28 January 2002 / Accepted: 30 September 2002
Published online: 28 November 2002

G.R. Spedding (✉)
Department of Aerospace and Mechanical Engineering,
University of Southern California, Los Angeles,
CA 90089-1191, USA

A. Hedenström, M. Rosén
Department of Animal Ecology, Lund University,
Ecology Building, SE-223 62 Lund, Sweden

We are grateful to the Knut and Alice Wallenberg Foundation, Carl Tryggers Foundation and the Swedish Natural Science Research Council for providing grants to obtain the equipment and for the Swedish visits by GRS (to AH). We are also indebted to both Colin Pennycuick and Thomas Alerstam for their friendly and generous support.

thousands of individual helium-filled soap bubbles, and it gave intermittent and nonuniform data coverage, with no guarantee of adequate data density close to features of interest or significance. Results were given in cross-sectional slabs of finite thickness cut through the three-dimensional data volume. Peak and gradient quantities were estimated from the most likely envelope of cross-section profiles, and no data interpolation was attempted.

Over the last 10 years, experimental fluid mechanics has experienced a dramatic emergence and increase in sophistication of digital particle image velocimetry (DPIV) methods, characterized by high and nominally uniform data density. These methods are quite robust because each elemental operation is an average over a large number of particles within a small interrogation box. They are also well positioned to profit from the predictable advances in speed, spatial resolution and affordability in digital micro- and optoelectronic devices. Useful reviews and summaries can be found in Adrian (1991), Westerweel (1993) and Raffel et al. (1998).

1.3
Opportunities

The successful design, development and practical use of a new low-turbulence, tiltable wind tunnel at Lund University (Pennycuick et al. 1997) has initiated a new period of high-quality steady animal flight data in repeatable conditions. The mean flow speeds (U=4–25 m/s) are moderately high by the usual DPIV standards. In particular, despite the convenience of the independently variable wind tunnel flow, the mean U component itself is uninteresting and inconvenient as it advects the wake past the measurement reference frame. This paper describes the development and deployment of a DPIV-based measurement system that compensates for the moving reference frame of the wake disturbance, and so allows measurements of bird wakes in air with an unprecedented degree of accuracy and reliability, and at moderate cost. Since the combination of method and application is new, and the objective is to make measurements of velocity and spanwise vorticity of known accuracy, the method is tested and validated rather thoroughly through a series of experiments whose complexity increases to eventually converge on the bird experiments themselves.

2
Materials and methods

2.1
Dual-camera system

Images are acquired on two digital CCD array cameras (Pulnix TM 9701 N) mounted side-by-side, with matched 17-mm focal length lenses (Schneider), each interfaced to a separate digital interface card (Imaging Technology IC-PCI-AM-DIG). The cameras are full-frame progressive-scan asynchronous-reset devices. The timing can be reset on either camera at any time ± 1 line scan time, which is 63.5 μs. Upon reset, either internal or external shutter or exposure can expose the entire frame simultaneously. Subsequently, the full frame is transferred to an on-camera frame buffer, where it remains available for transfer to the host PC. The reset operation is synchronized with the 10-Hz repetition rate of the laser, and each interface card transfers its frame memory through DMA transfer during this interval. The total number of frames is thus limited only by PC RAM, and is currently is equivalent to 150 frame pairs, or 15 s of data.

A Nd:YAG laser with 200 mJ/pulse (Quanta Ray PIV II, Spectra Physics) was used. Two four-channel delay generators (Stanford Research Systems DG 535) synchronize the acquisition timing with the laser pulses. One controls two Q-switches that determine the timing of the laser pulses, and the second, slaved to the internal clock of the first in basic repetition rate, controls the camera asynchronous reset. Seed particles were injected periodically by a commercial fog generator (the mean particle diameter was 1 μm) and were allowed to fill the wind tunnel completely by recirculation during the experiments. The fog is not so dense as to disturb the flying animal, and the introduction mechanism is downstream of the test section so as to avoid disturbing either the bird or the flow. The laser beam (d=8 mm) is collimated and then spread into a light sheet with selectable thickness and width by a sequence of plano–concave and plano–cylindrical lenses. Further technical details can be found in a joint USC/Lund University internal report, available from the authors.

2.2
Correlation imaging velocimetry

Sequences of digital image pairs were processed using a custom DPIV technique named correlation imaging velocimetry (CIV, Fincham and Spedding 1997). The basic principle is the standard DPIV computation of cross-correlations between small subwindows of successively exposed images. In CIV, the cross-correlations are variance-normalized and the computation is done directly rather than through fast Fourier transforms. Consequently, the interrogation boxes themselves can be of arbitrary size and shape. Furthermore, because the search radius of possible correlation calculations is set independently of the correlation box size itself, the boxes can be small, even when displacements are a large fraction of their linear dimension. Subpixel resolution of 1/50th pixel displacements are possible through an iterative correlation peak-fitting scheme with a thin-shell smoothing spline (Spedding and Rignot 1993). The same spline algorithms are then used to reconstruct velocities and their spatial derivatives on an arbitrary grid, correcting for the original displacement of the raw displacement calculation. Given a certain physical setup for particles and lighting, the only remaining physical control parameter is the effective DPIV exposure time δt, determined by the time between laser pulses. Time δt is normally adjusted so that mean displacements are on the order of 5 pixels, which is typically one-fourth of an interrogation box size. If the minimum uncertainty is 1/50th pixel, then the bandwidth of velocities is 1:250, and uncertainties of less than 1% can be claimed. Here the two images come from two different cameras, arranged side-by-side with the second exposure taken on the downstream side. This arrangement allows displacements from the mean flow to be removed, and so the 5-pixel criterion can be applied to the disturbance quantities alone. The

uncertainty estimates are thus applicable in a frame of reference in still air, through which the bird moves at mean speed U.

2.3 Calibration and analysis procedures

The simple and robust synchronization (28/30 frame times are available for image transfer to RAM), together with moderate cost of a two-camera system make it an attractive option for flows that require high-speed effective shuttering. The primary disadvantage is in the physical matching of the optical characteristics. The two optical axes will never be perfectly aligned, the two focal lengths will never be identical, and the cross-correlation will be measured between two different, and noncoincident, effective lens distortion curves. Nevertheless, the combined effects of all of the physical mismatches can be removed to quite high accuracy, by careful mapping of the apparent displacements of stationary control objects imaged by both cameras. The method for mapping the apparent pixel displacements of these objects is just the same as that used to map the fluid flow itself, so the calibration target is a pseudoparticle field, painted onto a flat surface. Apparent motion of this stationary surface shows the net contamination of the measured velocity field by geometric distortion and misalignment of the cameras and lenses. Since this is the only measured quantity, there is no other effect to correct for. The procedure is checked by calculating the motion of known calibration objects, primarily a spinning disk. The procedure is then repeated one more time to carefully measure and remove the mean flow properties in the wind tunnel, which are of no intrinsic interest. Thus the wake flow is truly measured as a disturbance quantity superimposed on the mean, which is not directly measured. The sequence is:

1. Compute the 'residual' flow from images of a stationary target. Misalignment of the cameras caused by the six possible relative translations and rotations and the mismatched focal length and lens distortion distributions are all bundled together and described as an apparent displacement field. This displacement field is removed by point-by-point subtraction. It is always calculated or re-calculated on the same grid as the real measurement.
2. Check the results from (1) by calculating the motion in translation and in shear of test objects. Most often this would be a stepper-motor-controlled spinning disk. The measured vorticity can be checked against the known rotation rate to accuracies of better than 1 part in 400.
3. According to the prescribed U value in a particular experiment, the initial DPIV exposure time δt between camera exposures is set so that

$$U\delta t = \Delta x_{1,2}, \tag{2}$$

the spacing between them. Ideally, a group of particles (associated with a measured fluid element) imaged at a particular position in camera 1 will be imaged at the same equivalent position (measured in pixels) in camera 2. This is subject, of course, to the modifications introduced in step 1. If the condition in Eq. (2) is not matched exactly, then there will be a nonzero mean flow in x. When this exceeds 1 pixel, the remaining mean ix integer pixel displacement in x is removed by cutting the left ix pixels from the left side of the left image and the same number from the right side of the right image. The effective image shifting is exactly equivalent to the operation in Eq. (2), and the dual-camera system preserves the number of pixels in x.
4. Measurement of $U,W(x,z)$, where U and W are time-averaged mean values of the undisturbed flow $\{u_i,w_i\}$ at each (x,z) measurement location:

$$\left.\begin{aligned} U(x,z) &= \tfrac{1}{T}\sum_{i=1}^{T} u_i(x,z), \\ W(x,z) &= \tfrac{1}{T}\sum_{i=1}^{T} w_i(x,z). \end{aligned}\right\} \tag{3}$$

The mean flow field in the wind tunnel is characterized as the background field in which the bird will operate.
5. Add bird. Following the removal of all mean displacement values of greater than 1 pixel, the CIV calculation proceeds on the remaining fluctuation values, defined as:

$$\left.\begin{aligned} u(x,z) &= U(x,y) - u_i(x,z), \\ w(x,z) &= W(x,y) - w_i(x,z). \end{aligned}\right\} \tag{4}$$

Finally, analytic differentiation of the spline coefficients at the same grid nodes gives the normal vorticity component

$$\omega_y = \frac{\partial w}{\partial x} - \frac{\partial u}{\partial z}. \tag{5}$$

quantity ω_y will also be referred to as the spanwise vorticity. Note how these quantities are all calculated pointwise, over the whole displacement field. The displacements of the fluctuating quantities are small, and the accurate estimation of these displacements is precisely the principal strength of the CIV method. For convenience, within this manuscript, the collection of methods in this list culminating in 'add bird' will be referred to as BPIV.

2.4 Bird flight performance and training

The test bird was an individual thrush nightingale (*Luscinia luscinia*). *L. luscinia* is an autumn migrant, flying from Europe to southeast Africa (Moreau 1972). It also habitually migrates at night, so flying in low light is not only unproblematic but natural. Four individuals were started in a training program but it quickly became clear that one would be a much more reliable performer. The main body measurements are given in Table 1, and characteristic dimensionless parameters are given in Table 2. As discussed in Sect. 1.1, we note the values of reduced frequency k not much less than 1 and Reynolds numbers are of order 10^4.

The bird was trained to fly close to the geometric center of the beginning of the wind tunnel test section by starting

Table 1. Morphological data for *Luscinia luscinia*

		Units	Mean value	Uncertainty
Semispan	b	cm	12.6	0.5
Wing area	S	cm^2	116	2
Mean chord	c	cm	4.6	0.2
Aspect ratio	AR	–	5.5	0.3
Body mass	m	g	30.5	0.5
Wing loading	Q	$N\ m^{-2}$	26	0.6

Table 2. Dimensionless numbers at low and high flight speeds

Flight speed (m/s)	U	5	11
Reynolds number	$Re=Uc/\nu$ ($\times 10^4$)	1.5	3.4
Reduced frequency	$k=\omega c/U$	0.75	0.32

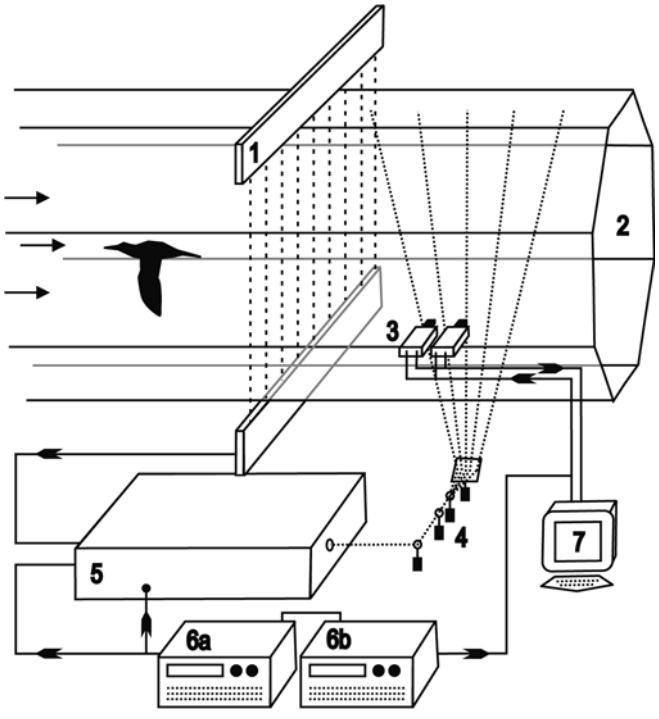

Fig. 1. BPIV. The bird flies freely near the front of the open test section (2). Behind, the wake is illuminated by a light sheet generated by pulsed Nd:YAG laser (5). The pulse intervals are controlled by timing boxes (6), which also generate the synchronization signals for the camera pair (3). First the upstream and then the downstream camera arrays are exposed, and digital mages are acquired directly into separate digital interface cards and then to PC RAM (7). If the bird strays back too close to the light sheet, then one or more beams of an infrared photodiode–LED (1) matched array pair are interrupted, and the laser pulsing stops immediately

from a perch about 10-cm upstream of the final flight position. The overall setup is shown in Fig. 1. The perch tip was located 5-cm beneath and 50-cm downstream of a stationary marker whose tip contained luminescent material. In reduced light, this is the most obvious visual reference point, and when the perch (whose tip was also luminous) was removed, flight would tend to occur in the general neighborhood of this point. As training progressed, the flights would lengthen, from an initial 5–10 s, to 30 s or more duration. The full training sessions also involve continuous, uninterrupted flights of 2–4 h as the bird would become accustomed to flying in the wind tunnel.

For 2 months prior to the experiments, conditions would gradually approach that of the real experiment. Flashing laser sheets and fog particles were introduced cautiously and for initially short periods. Flying in close proximity to high-energy laser pulses could be hazardous, and so a vertical grid of infrared LED–photodiode pairs was constructed to automatically suspend pulse output when any part of the grid was interrupted. The laser output is inhibited by suppression of the Q-switch timing pulses, which does not suspend the regular lamp trigger mechanism, required for stable regular output. The reset must always be a manual reset, to avoid unpredictable restarts.

The experiments themselves ran on most weekdays over a 4-month period from September to December (inclusive), typically for one or more individual sessions of about 2 h, with multiple repetitions of a single flight speed (mean wind tunnel flow speed U) in each session. Mean wind speed U was the only parameter that was varied during the 4-month experiment period, although there were slight changes in the experimental protocol to encourage stable, repeatable performances.

Free-flight (albeit constrained in a wind tunnel) experiments are difficult because the subject location is hard to know precisely. In these experiments, the measured wake itself is used to estimate some of the variables. The position in y (lateral or cross-stream location in the test section) was checked by simultaneously taking standard video from a camera positioned downstream of the test section. The electronic shutter was kept open, and the lens was covered with an optical filter to remove most of the energy at 532 nm. The frame rate is 50 Hz, which is 5 times the laser pulse repetition rate. No great effort was made to synchronize the two systems as the likelihood of flashes being recorded was sufficiently high. The operators of the experiment recorded additional information onto the audio track. The images show a bright vertical line (the laser sheet) and a silhouette of the bird in flight. The location of each flash with respect to the wingspan can be estimated, and then matched with DPIV data records (raw image sequences).

Individual flights may not be completely steady, but there can be small accelerations, turns and climbs; these occasions can be checked on the rear-view video. The flapping frequency of the thrush nightingale is close to, but not the same as, the 10-Hz laser repetition rate. Thus each continuous image-pair sequence gives velocity fields that are almost phase-locked with the wingbeat, but with a small shift. This is extremely convenient because it allows the wake to self-sample, since gradually different portions of the wake appear in front of the camera. Moreover, if the wake structure is repeatable during each sequence, and if the wake does not appear at different vertical locations, then the flight can be verified to be steady and level. The exceptions also proved to be very informative, as the consequences of changes in a wake pattern at one

time-step could be seen in the next, roughly one wingbeat later. An example of such a time sequence will be given in the results.

3
Results

3.1
System tests and calibration

3.1.1
Static camera and lens calibration

For this section devoted to camera/lens characteristics, we temporarily adopt a coordinate system attached to the camera system, where x and y run horizontally and vertically, respectively, and u and v are the velocity components in the x–y plane. Figure 2 shows the apparent displacement field from the optical distortion and misalignment for a fixed object placed in the wind tunnel test section. The displacements are calculated from the CIV algorithms, and those shown are the average over ten frame pairs. The variation within the ten frame pairs is insignificant. The pattern can be viewed as a superposition of two axisymmetric and similar lens distortion functions, whose centers are displaced from each other in x. This pattern is observed when the lens axes are very close to parallel, and the cameras are level. In that case, the mean values of both u and v are close to zero.

The measurement of a mean u- or v-component is used as a diagnostic in aligning the cameras. The variation in both u and v across the field of view is smooth, and may be 1.5 pixels in total magnitude. Such a pattern can quite confidently be modeled with a simple interpolating function such as a third-order polynomial, which is shown for $u(x,y)$ in Fig. 3. The characterization of the residual velocity field in this way allows straightforward treatment of real images by subtraction with a function whose maximum complexity reflects the physical origin of the distortion surface.

A careful inspection of the residual field shows two slightly unsmooth locations in the original interpolation surface that one would not wish to propagate into the correction field. The polynomial approximation indeed lacks these features.

3.1.2
Timing tests with spinning disks

A stepper-motor-controlled spinning disk placed in the wind tunnel test section was illuminated on its face by the pulsed laser. The disk face was painted to resemble particle images on a black background, and the angular rotation rate Ω was measured in two series of experiments. In the first, δt was tuned to Ω (higher values of Ω were measured with shorter exposure times δt), and the measured rotation rate was the averaged measured out-of-plane vorticity over the entire velocity field. The result in Fig. 4 shows

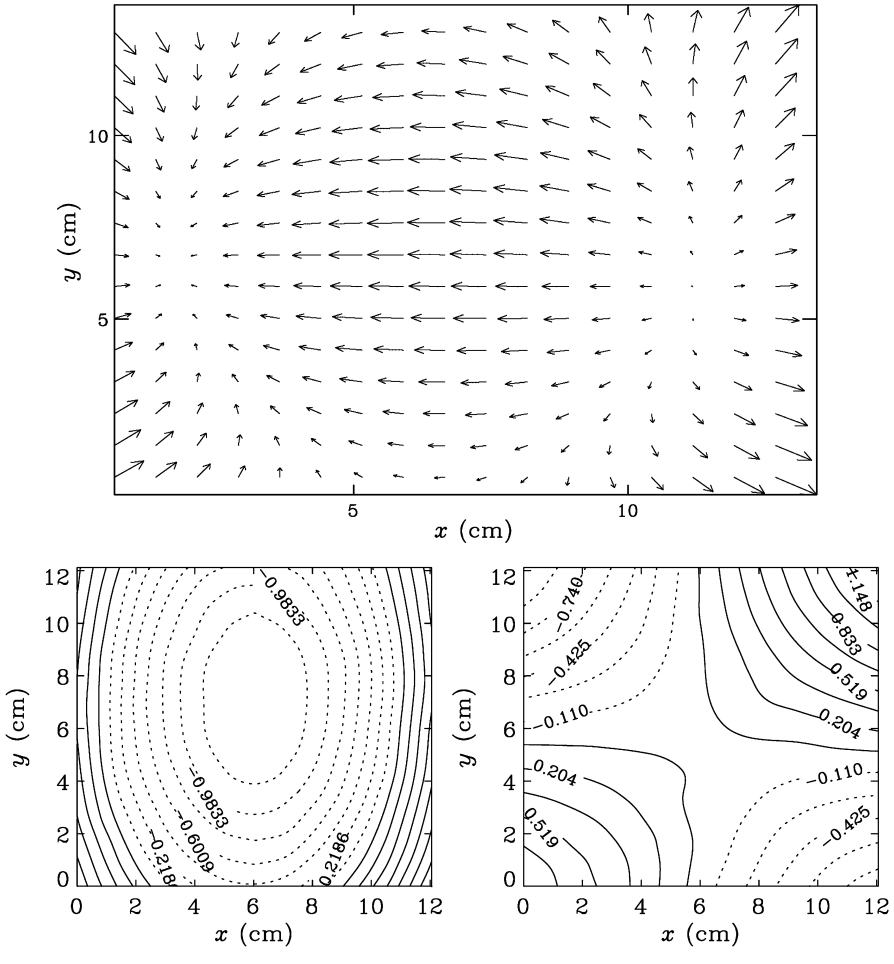

Fig. 2a–c. Apparent velocity field $u(x,y)$ from geometric and optical misalignment and distortion. The length of the vector arrows in (a) is arbitrary, but the u- and v-components are shown in units of pixel displacement at a focus length of 60 cm in (b), (c). In this figure $\{u,v\}$ displacements are in $\{x,y\}$ in the camera reference frame, where x is horizontal and y is vertical

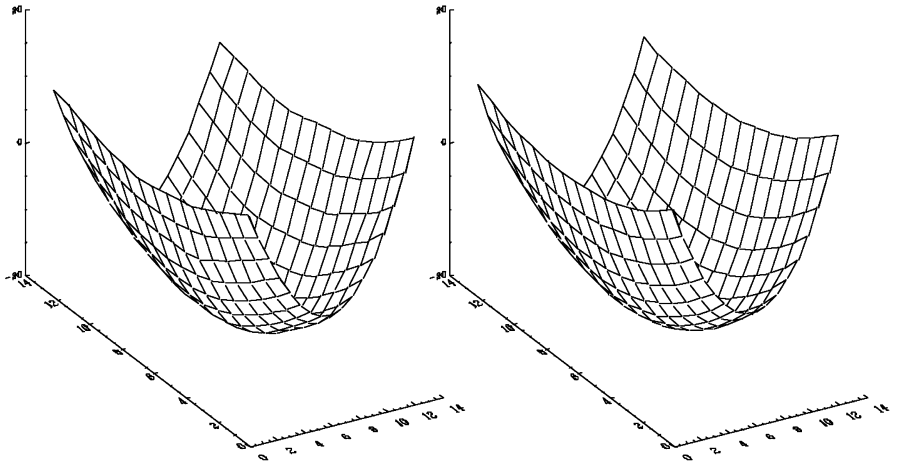

Fig. 3. The u-component of the residual field (*left*), and its approximation by a third-order polynomial interpolating function (*right*)

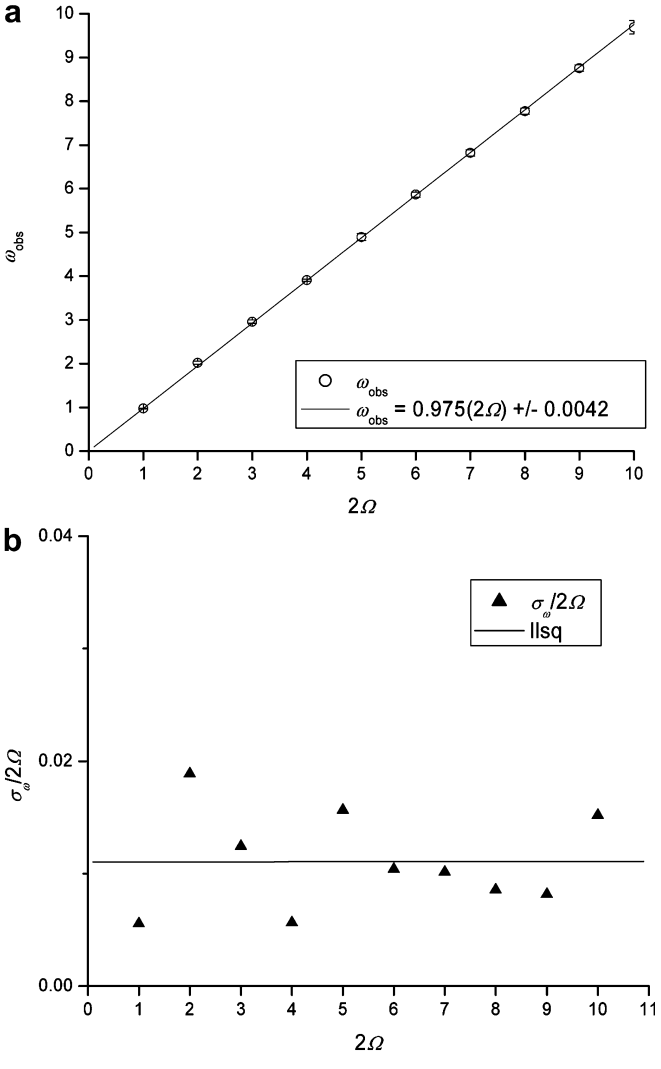

Fig. 4. **a** Measured disk rotation rate as function of prescribed rotation rate 2Ω; **b** normalised variation in ω_{obs}. The linear least squares fit (llsq) cannot be distinguished from a flat line

that Ω can be measured accurately and reliably, and also that the uncertainty of the measurement does not vary with Ω. The normalized standard deviation σ_ω is constant at approximately 0.01, or 1%. The result is expected, since the calculation error in the CIV algorithms is fixed in pixels. When displacements are held to similar values, through variation of δt as Ω varies, then, in the absence of any further systematic measurement errors, the uncertainty in ω_{obs} will be constant. A reasonable interpretation of Fig. 4 is that extraneous errors have been reduced to insignificant levels in this measurement.

The second measurement tests were designed to make a more realistic estimate of the likely measurement uncertainty of instantaneous vorticity fields. Here, the exposure time is held fixed, as it must be in any single frame-pair. (There are techniques for calculating multiple timescales from different exposures centered at the same time, but they will be ignored here.) In Fig. 5, the variation in measured ω is plotted as a function of 2Ω for three different δt values.

When Ω is small (δt=1 ms), the measurement uncertainty is dominated by the algorithm error. As Ω increases displacements also increase, and the relative uncertainty decreases to values of around 10%. This is much larger than the previous measure because it takes into account all instantaneous spatial variations in ω_{obs}.

For larger δt (δt=5 ms), the relative uncertainty is within the range 0.05–0.1 over almost an order of magnitude variation in Ω. This is the performance that one would aspire to through properly selected values of δt in a real experiment. For the largest exposure time (δt_1=10 ms), σ_ω increases after 2Ω =4, primarily showing that as displacements grow very large the correlation amplitude decreases. It does this partly by deformation of the correlation box itself – an effect that can quite readily be compensated for. In practice the primary contributor to the loss of correlation at large pixel displacements is the loss of particles from the two-dimensional interrogation plane, rendering local deformation corrections somewhat superfluous.

3.2 Mean and turbulence quantities in the background flow

The basis of the BPIV method is to treat all background disturbances, mean flow and lens distortions alike, as some mean vector field that will be removed, pointwise, from the final result. Before discarding all such information, it is reasonable to check the flow and its measured values. The quantities of interest are (recall the notation in

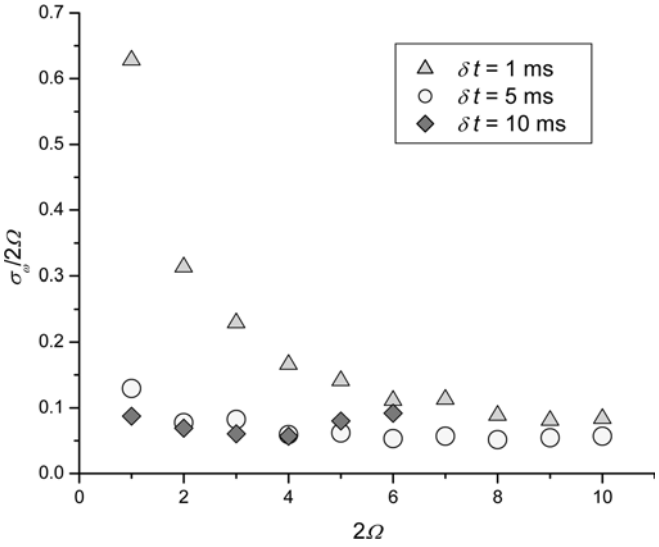

Fig. 5. Normalised mean spatial variance in measured rotation rate for three fixed effective exposure times

Eq. (4) where $u(x,z)$ and $w(x,z)$ are instantaneous disturbance quantities) the streamwise-averaged velocity profiles

$$U_X(z) = \frac{1}{n_x}\sum_{i=1}^{n_x} u_i(x,z), \tag{6}$$

where n_x is the number of mesh/data points in the x-direction; the globally averaged values of U and W

$$\left.\begin{aligned} U_0 &= \tfrac{1}{n}\sum_{i=1}^{n} u_i(x,z), \\ W_0 &= \tfrac{1}{n}\sum_{i=1}^{n} w_i(x,z), \end{aligned}\right\} \tag{7}$$

where $n=n_x n_y$ is the total number of data points; the root-mean-square (rms) of the fluctuations

$$\left.\begin{aligned} u' &= \tfrac{1}{n}\left\{\sum_{i=1}^{n}\left[U_0 - u_i(x,z)\right]^2\right\}^{\frac{1}{2}}, \\ w' &= \tfrac{1}{n}\left\{\sum_{i=1}^{n}\left[W_0 - w_i(x,z)\right]^2\right\}^{\frac{1}{2}}, \end{aligned}\right\} \tag{8}$$

and their magnitude

$$q = \left\{u'^2 + w'^2\right\}^{\frac{1}{2}}. \tag{9}$$

Figure 6 shows profiles of $U_X(z)$ for the entire operable wind tunnel range of U_{set}. Quantity U_{set} is the set value of the wind tunnel speed, which is determined by readings from a pitot–static tube at the tunnel wall. The uncertainty in U_{set} is ±0.2 m/s. Over the observation window the profiles are mostly flat, and the measurement scales with U_{set} as it should. The source of the inflection at z=15 cm for $5 \le U_{\text{set}} \le 15$ is not known, but it is small enough to be ignored. Figure 7a shows that the measured magnitudes of mean flow quantities are correct according to the control instrumentation. This covers the usable range of the wind tunnel, and also the range of likely speeds of birds in aerobic flight. In Fig. 7b, the magnitude of the measured

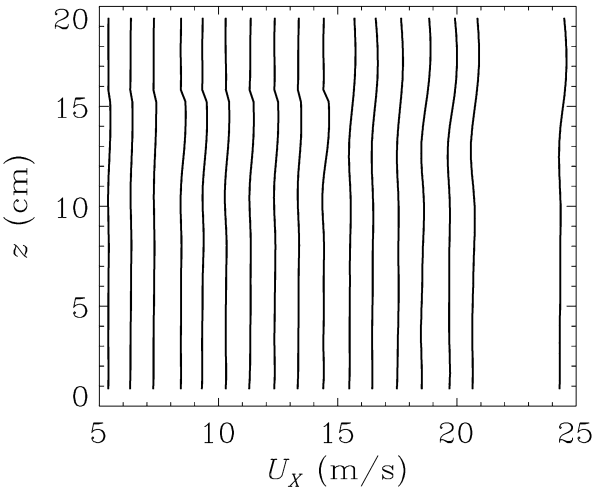

Fig. 6. Streamwise-averaged velocity profiles calculated from CIV for U_{set}=[5, 24] m/s

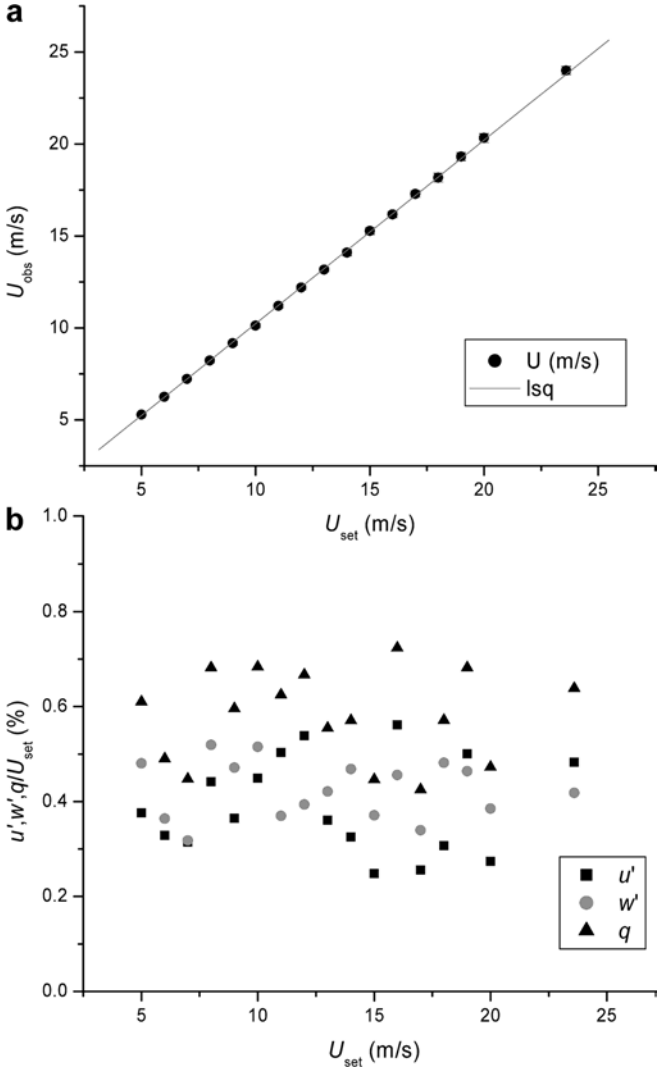

Fig. 7. **a** Mean measured flow speed vs. nominal set speed; **b** measured turbulence intensities in the undisturbed mean flow

rms velocity fluctuations is shown to be isotropic in $\{x,z\}$, independent of U, and to have values around 0.5%. This greatly exceeds the average values of 0.04% measured in

the initial calibrations with constant-current hot-wire anemometry. A quick calculation shows why. The optimized CIV algorithms are claimed (Fincham and Spedding 1997) to have a resolution of 1/50th pixel. When mean displacements are set at approximately 5 pixels, as they are here, then the uncertainty is 0.4%. Thus the variance in Fig. 7b is indistinguishable from measurement noise. The effective resolution can be improved only by increasing δt. Figure 8 shows how the measured rms turbulence intensities are strongly dependent on δt. The measured turbulence intensities can be approximately halved to 0.25% by increasing δt. The true turbulence levels in the wind tunnel are not measurable with the current technique over this range of scales. Figures 7b and 8 do show the likely noise floor for operating conditions close to the real bird experiments. They indicate that turbulent fluctuations in the wake of around 0.5% should be measurable. The spinning disk experiments (Figs. 4 and 5) indicate that in the presence of shear, properly-tuned acquisition parameters will allow vorticity measurements with errors less than or equal to 10% of the local value.

3.3
Vortex wake of a fixed airfoil

The objectives of the bird experiments are to measure wake quantities with the required accuracy to calculate integrated wake momentum values in the principal directions (x and z), and to estimate vorticity distributions in the wake to check and explore various possible wake-modeling strategies. As proof of concept, the strategy was deployed on a fixed airfoil of finite span, mounted to a single-pan balance to check approximate vertical force magnitudes. The airfoil parameters are given in Table 3. The overall dimensions were chosen to resemble those of a single bird wing. The cameras were positioned so that the left margin of the right camera was aligned with the trailing edge of the airfoil; consequently, the first data point occurs one-half a grid mesh, or about 1.7 mm, downstream of this point.

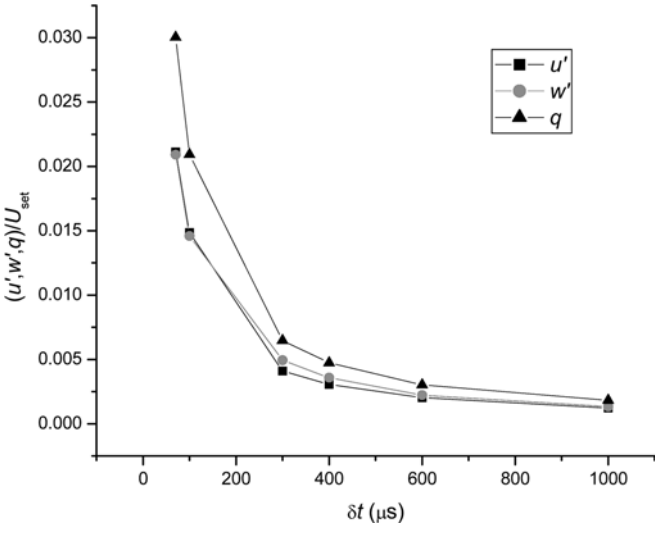

Fig. 8. Variation of measured turbulence intensities with DPIV exposure time δt

Table 3. Geometry of the fixed airfoil experiment

Mean speed (m/s)	U	8.6
Span (cm)	$2b$	17.0
Chord (cm)	c	5.1
Max. thickness (cm)	t	0.61
Re	Uc/ν ($\times 10^4$)	2.9
AR	$2b/c$	3.4
TR	t/c	0.12

Figure 9 shows the spatial distribution of the fluctuating streamwise velocity component $u(x,z)$, the spanwise vorticity $\omega_y(x,z)$ and its time-averaged value $\bar{\omega}_y(x,z)$ for four different angles of attack α. The data are plotted on a ten-level color bar, whose resolution thus corresponds approximately to the worst-case resolution in ω_y. The vorticity maps are balanced around zero value in the middle of the color bar, while the $u(x,z)$ measurements have maximum value zero and minimum value rescaled to the black color block on the left of the bar. At close to zero angle of attack, the wake defect is small in amplitude (low drag), and shows signs of a laminar instability. The nonuniform distribution of vorticity is evident over the

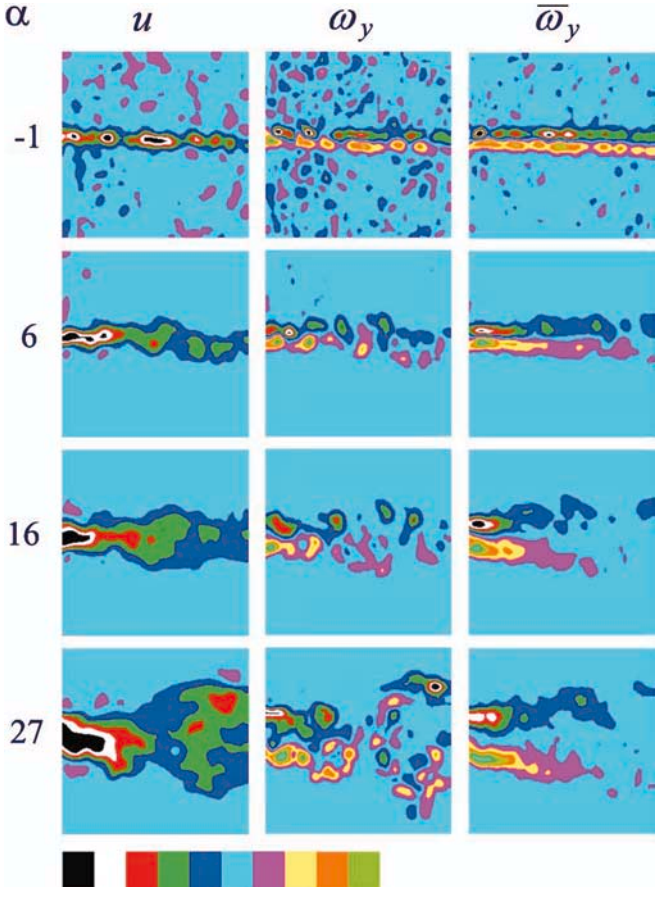

Fig. 9. Instantaneous wake defect u (*left column*), spanwise vorticity ω_y (*middle column*) and mean spanwise vorticity (*right column*) for fixed rectangular wing at four different angles of attack. Mean flow is from left to right. U=8.6 m/s and Re=2.9×10^4. The observation box dimensions are $\Delta x/c$=3.84 and $\Delta z/c$=3.60 in the horizontal and vertical directions, respectively. The left margin coincides with the trailing edge of the airfoil

whole wake, in both upper and lower shear layers, even at this lower angle of attack.

As α increases (6), the wake defect magnitude increases, and a longer wavelength mode is apparent. The individual vortex structures still have approximately the same size and spacing as in the low-α case. With further increases in α (16, 27), the initial wake thickness increases and so does the spreading rate as shear layers formed by separation from both leading and trailing edges become unstable separately. In the time-averaged view the two shear layers appear almost independent, but in the instantaneous data it is clear that the wake structure is still unified by the larger-scale high-amplitude oscillations. The magnitude of these leads to large variations in u and ω_y far outside the mean wake.

There are few investigations of low-*Re* airfoils in the literature and none that deduce the airfoil characteristics from wake surveys such as this one. This is partly because it is much simpler to measure force components directly, but here the exercise is of interest also as it pertains to bird wake measurements, where direct measurement is not an option. Figure 10 shows the increase and saturation of the peak vorticity, of either sign, with angle of attack. Each measurement is repeated for 20 separate time-steps at each α, and the error bars show the standard deviation. At low α, the upper and lower shear layers have very similar peak values, but the upper shear layer becomes slightly stronger at intermediate α. Although the variation between samples is larger than this difference, it shows that a net circulation, and hence net lift, can be deduced for the airfoil itself. The variation suggests that calculating this from single time-step measurements would be very difficult because of the complicated spatial structure and organization of the wake vortices. For α 16 (see Fig. 9), the peak vorticity increases no further, as the strongly separated flow is very disorganized and small-scale turbulence has disrupted the coherence of the wake.

A simple force balance calculation can be made from the airfoil data of Fig. 9. More thorough derivations can be found in standard texts (e.g. Anderson 1984), but very briefly, the x-momentum equation can be integrated over a control volume that includes all disturbances to a mean uniform flow, at speed U_0, to give the drag force per unit span D' in terms of the velocity defect $u(z)$

$$D' = \rho U_0^2 \int_{-h/2}^{h/2} \{u(z) - u(z)^2\} \mathrm{d}z. \tag{10}$$

The example is for a two-dimensional uniform flow, integrated over a box of height h. The integral in Eq. (10) has dimensions of length and can be conveniently denoted

$$\theta = \int_{-h/2}^{h/2} \{u(z) - u(z)^2\} \mathrm{d}z, \tag{11}$$

and so the total drag force over the span $2b$ is

$$D = \rho U_0^2 2b\theta. \tag{12}$$

The drag itself is most conveniently expressed in terms of a drag coefficient C_D

$$D = \frac{1}{2}\rho U_0^2 S C_\mathrm{D}, \tag{13}$$

where S=2bc is the wing planform area, and finally C_D can be written

$$C_\mathrm{D} = \frac{2\theta}{c}. \tag{14}$$

The velocity profiles $u(z)$ can be calculated either as mean values from a number of single vertical transects through an instantaneous velocity field, or as mean values from a mean field taken from a number of time-steps. The drag coefficient is determined completely by the magnitude of the velocity defect, normalized by the only reference length in the problem, the wing chord.

Figure 11 shows C_D as a function of angle of attack α for the fixed airfoil. The absolute values of C_D are much as expected for a streamlined body ($C_{\mathrm{D,min}}$=0.012 at α=–1), and at small α the different methods for calculating C_D agree. The value of C_D rises as α increases, and the difference between calculations based on instantaneous and

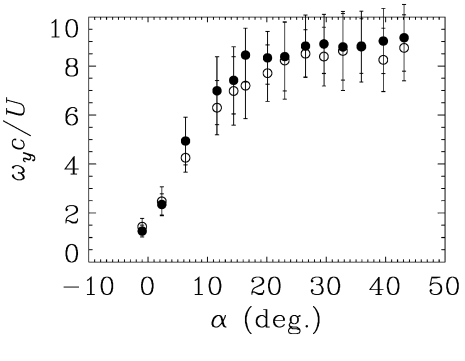

Fig. 10. Maximum values of ω_y versus angle of attack for fixed airfoil. Mean values for upper and lower shear layers are shown in *closed* and *open circles*, respectively. The upper shear layer has negative sign and so the absolute value is plotted here. The error bars show the standard deviation of the peak spanwise vorticity over 20 separate time-steps

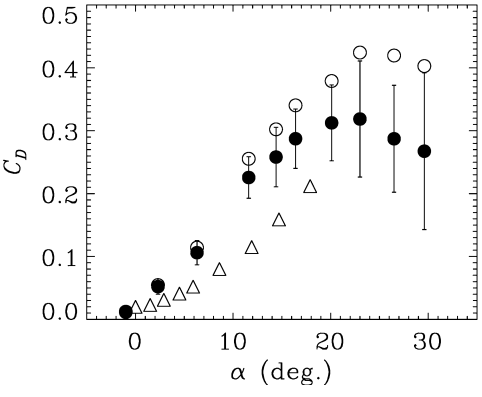

Fig. 11. Drag coefficient α calculated from wake defect for fixed airfoil. *Open circles* are from time-averaged wake, and *solid circles* are averaged from all vertical columns in instantaneous {*u*,*w*} fields. The *open triangles* are taken from classical data of Prandtl and Tietjens (1934, p. 209) for the comparable *AR*=3 wing, but at higher *Re*

mean fields also increases. This is due partly to the increased unsteadiness in the wake itself, and partly to the increased magnitude of three-dimensional disturbances, either from instability and turbulence in the wake or from the encroachment of spanwise velocity components from the tips of the finite wing/wake. Indeed, at moderate aspect ratios (AR), i.e. AR=3.4, these effects are quite strong. The comparison with classical force-balance data (open triangles) shows a significantly higher calculated drag for similar AR, but here Re is about two orders of magnitude lower and such differences must be expected. The problem of low-Re operation has already been noted in Sect. 1, and the effects of premature separation of marginally stable viscous boundary layers are evident.

3.4
Vortex wakes of flying birds

The BPIV method was very successful and robust in application to bird wakes, where turbulence levels and three-dimensional motions through the light slice were of sufficiently low amplitude to allow exposure times δt around 300 μs. For this case, data on the measurable 'turbulent' fluctuations in Fig. 8 suggest a resolution of better than 0.5% in u and w.

Figure 12 is a cross section just off the center-plane through a single wake structure deposited during the course of one downstroke of the thrush nightingale flying in level, steady flight at 5 m/s. A strong downflow can be seen between two counter-rotating vortex structures. The corresponding downward momentum flux represents the weight support component of the overall force balance. In Fig. 12b the spanwise vorticity distribution can be seen to be quite complex, although concentrated mostly in the two rotating elements observed in Fig. 12a. Helmholtz's laws require that vortex lines terminate either at boundaries or in closed loops, so if there are no other strong concentrations of vorticity, then Fig. 12 must represent a cross section through a closed vortex loop, as originally modeled by Rayner (1979a, 1979b), and subsequently confirmed in experiment (Kokshaysky 1979; Spedding et al. 1984; Spedding 1986) for birds in slow flight, and by Rayner et al. (1986) for noctule bats.

Nevertheless, if the single closed-loop topology for the configuration of vortex lines in the wake is a most nearly correct description, the more diffuse concentrations of vorticity in the cross section through the stopping vortex from the end of the wingbeat are very repeatable in these experiments, and are far above measurement noise. The peak positive vorticity in the starting vortex is 920 s^{-1}, and in the negative stopping vortex it is –250 s^{-1}. The uncertainty in the measurement is approximately ±20 s^{-1}. This asymmetry in starting and stopping vortex structures was previously noted and discussed by Spedding (1986), but quantitative details were not given.

A single time series of seven consecutive wingbeats, captured over six time-steps, shows further interesting complexities in the wake structure for a sequence that includes a slow climb. The data in Fig. 13 are shown as $\{u,w\}$ vector fields and their corresponding spanwise vorticity distributions, plotted on the same ten-step color bar used for the fixed airfoil. The spanwise location is

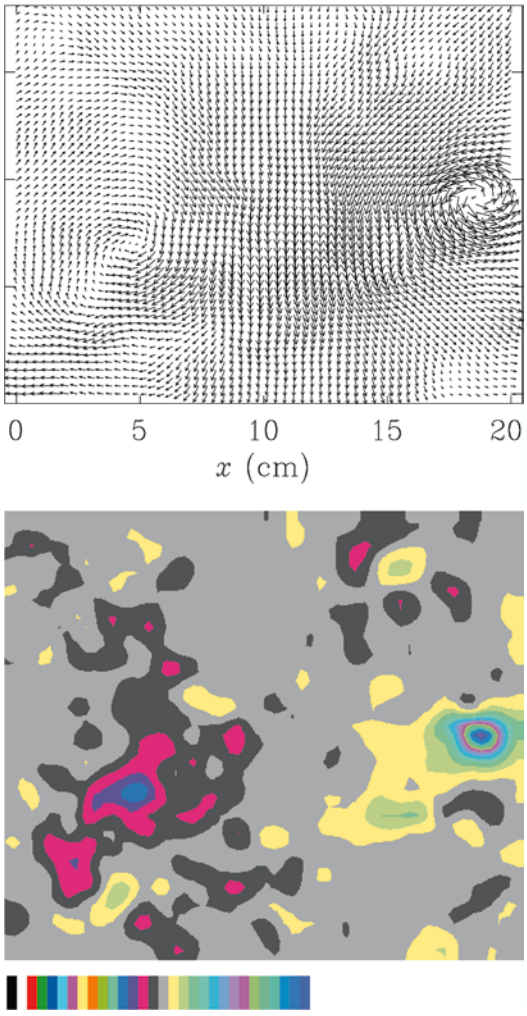

Fig. 12a, b. Vortex wake from downstroke of thrush nightingale flying at 5 m/s: **a** velocity vector field $\{u,w\}(x,z)$; **b** $\omega_y(x,z)$ scaled symmetrically about a stepwise color bar with 30 increments. The negative-signed (clockwise) stopping vortex is much weaker and more diffuse than the starting vortex

about halfway between center-plane and midwing. Figure 13a begins with a section through a clearly defined starting vortex, accompanied by a secondary weaker patch of vorticity of the same sign to the lower left. The strong downwash is as previously noted in Fig. 12, and the downstroke-generated structure is preceded (in time, or to the right of the picture) by mostly nothing. This too is an interesting result, supporting the notion of an inactive upstroke at this speed. Figure 13b is 1/10th s, or about 1.2 wingbeats later. The induced flow of the primary starting vortex can be seen at the right-most edge of the picture, and the height (z-location) is close to the previous structure, as judged by the change in sign of the u velocity component. The secondary vortex can be identified in the $\omega_y(x,z)$ plot. Following the pattern in Fig. 12, the negative-signed vorticity is not arranged in so compact a form, and there are concentrations that trail into the upstroke. Continuing into Fig. 13c, a quite complex pattern is seen, and there are coherent disturbances attributable to the upstroke that rise far above the noise. The interpretation at this point is not obvious, but something different from

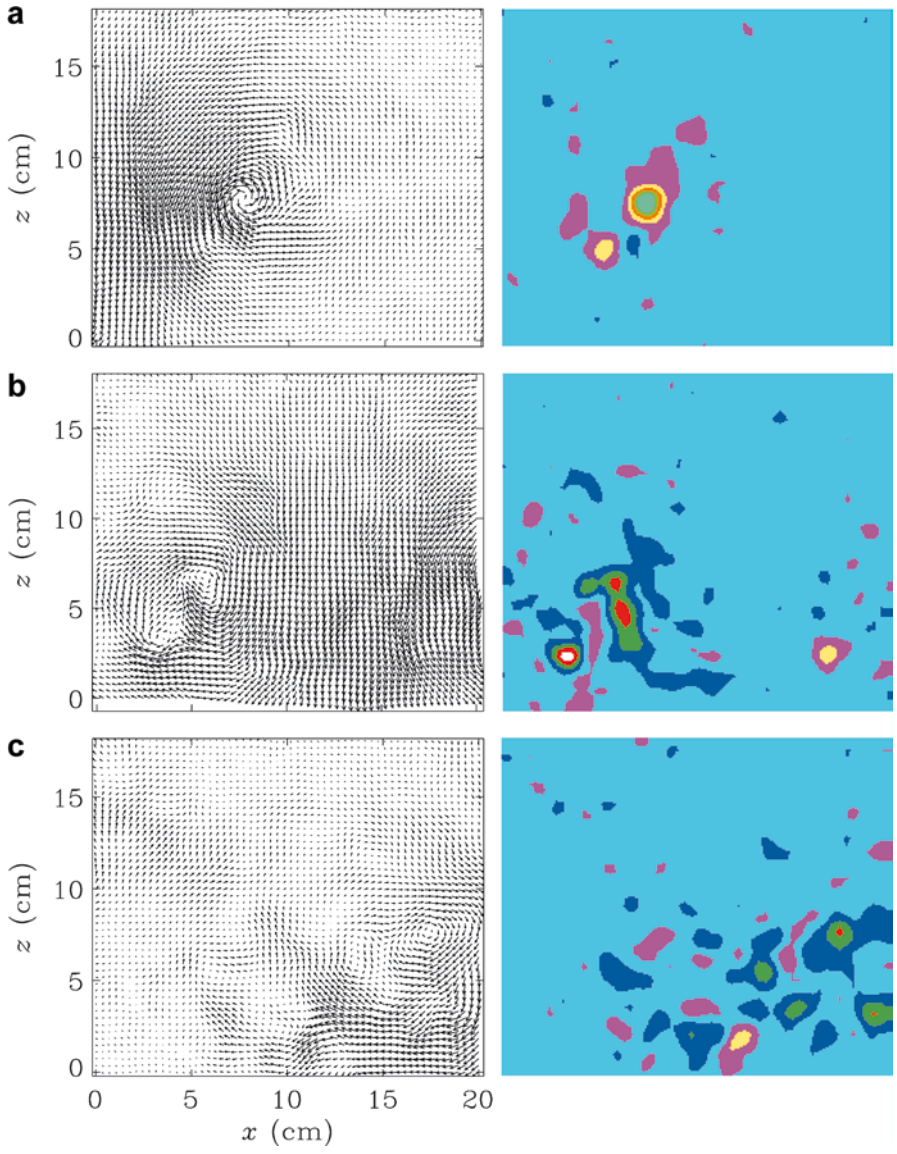

Fig. 13a–f. Velocity vector fields $\{u,w\}(x,z)$ (*left column*) and spanwise vorticity $\omega_y(x,z)$ (*right column*) for six consecutive time-steps for a thrush nightingale flying at 5 m/s. Spanwise vorticity ω_y is shown on a ten-step color bar as in Fig. 11 for the fixed airfoil. The vorticity maps are scaled onto the color bar according to constant global limits at $\omega_y c/U \pm 5.5$. Figures 13a (*top row*) and 13b (*bottom row*) show two consecutive time-steps. The sequence is continued in Fig. 13c–f

steady level flight is occurring. In the next frame (Fig. 13d) it becomes clear that the bird has risen about 5 cm, as judged by the higher z-position of the next starting vortex. The approximate equivalent horizontal distance is $\Delta X = U_0 \Delta t$, where $\Delta t = 2 \times 0.1$ s, so $\Delta X = 1$ m, and the climb angle is 1:20, or 3°. The usual diffuse stopping vortex pattern is resumed in Fig. 13e, followed by an inactive upstroke. Finally, the last frame (Fig. 13f) shows the empty space between successive stopping and starting vortices, again confirming the inactive upstroke, and hence the closed-loop topology of the wake.

Figures 12 and 13 are examples of detailed vorticity maps and of phase-shifted time series that have far greater spatial resolution and much improved accuracy over any previous animal flight application in reconstructing velocity vectors and their spatial derivatives. In particular, the CIV correlation parameters have been tuned to ensure correct estimates of peak vorticity in cross sections through wake structures, and Fig. 14 shows the peak positive and negative spanwise vorticity measured in the sequence of Fig. 13. The positive peaks are about twice the magnitude of the negative peaks, whose values appear out of phase because the sampling in this particular sequence tends to show first one, and then its opposite-signed counterpart in the following frame (from the next wingbeat), rather than both simultaneously (as in Fig. 12). The two peak values of $\omega_{y,\max}$ are 840 and 900 s^{-1} (± 20 s^{-1}). This is much higher than the only previously reported values of 480 and 120 s^{-1} for a pigeon and jackdaw, respectively, in slow flight (Spedding et al. 1984; Spedding 1986), suggesting that resolution problems in older data might lead to some revision of the quantitative arguments stemming from it.

4 Summary and conclusions

The BPIV technique works very well for the bird flight problem. The procedure for using the CIV (or general DPIV) algorithms to map successive levels of distortion and/or background flow is quite general and flexible. Here it allows the distortions introduced by the hardware image shift to be removed, and so the comparatively inexpensive and robust two-camera system can focus on the real fluid flow induced by test objects. The spatial

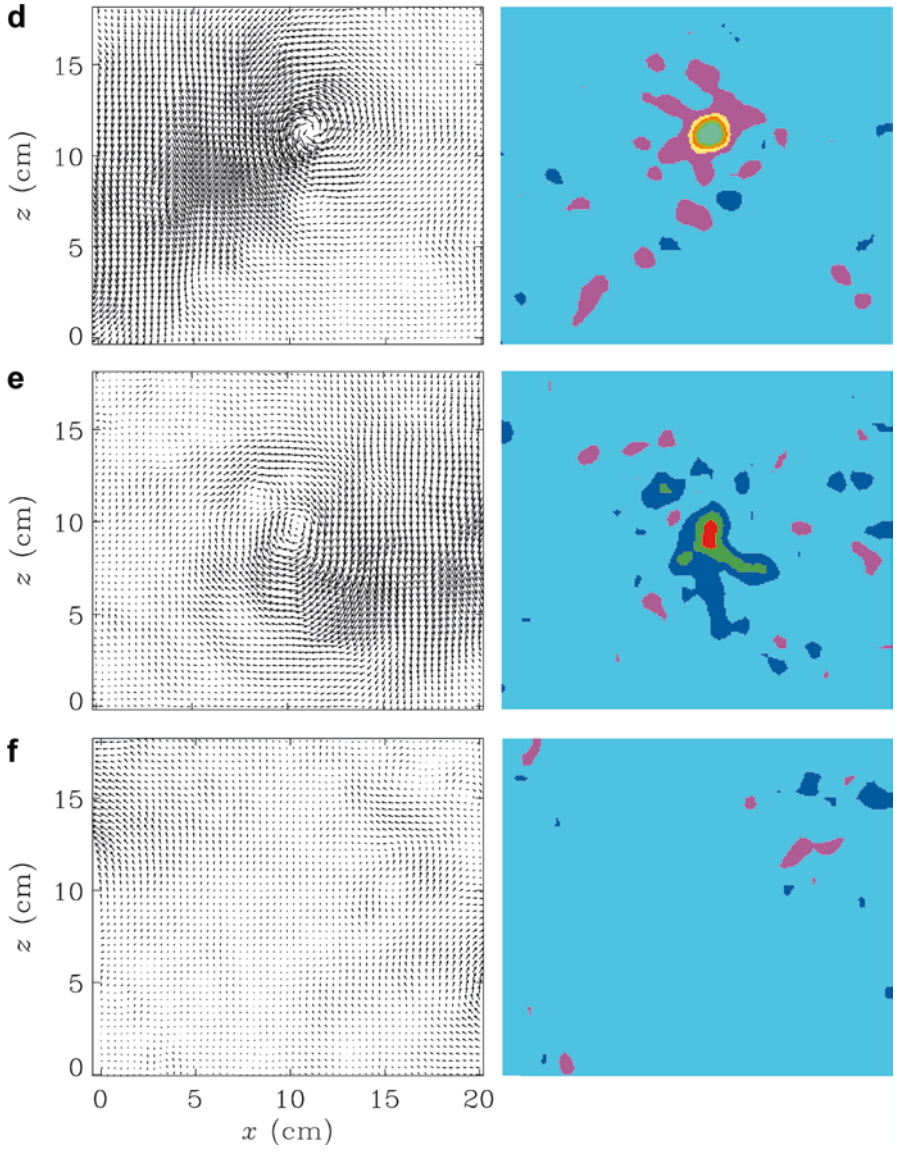

Fig. 13a–f. (Contd.)

resolution is 0.35 cm, or about 8% of the mean chord, and the measured uncertainties of both fixed and moving background objects suggest that the method can resolve $\{u,w\}$ fields to within 1% and gradient quantities such as ω_y to within 10% of their real value.

The wake measurements of the fixed rectangular planform airfoil show that complex structure can occur even for simple geometries, which can render estimates of derived quantities uncertain. The uncertainty in correctly accounting for complex wake structure can be much larger than the basic numbers quoted above for velocity and vorticity fields. However, the measurements also show that such estimates can be made, provided they are within the appropriate conceptual framework.

At slow forward flight speeds, the structure in the thrush nightingale wake is quite well accounted for by a model of closed vortex loops, one shed per downstroke, and with effectively nothing happening on the upstroke. However, detailed quantitative surveys show a persistent asymmetry in the concentration of starting and stopping vortices. The former have vorticity magnitudes that are about twice as large as have been previously reported,

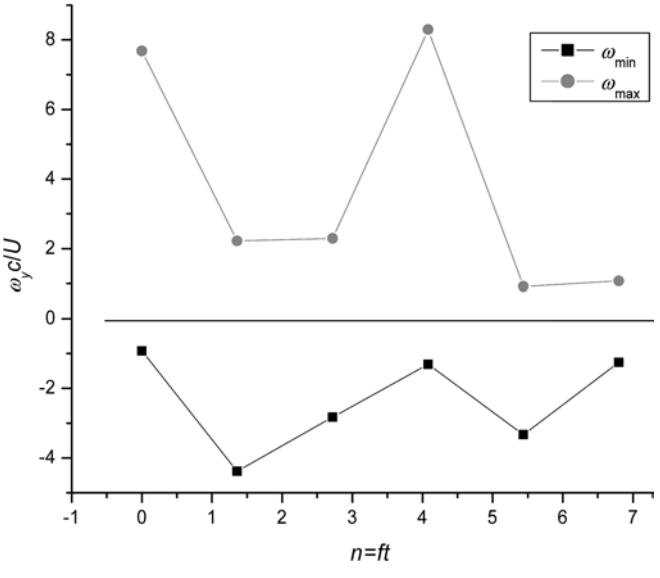

Fig. 14. Values of minimum and maximum measured vorticity in the thrush nightingale sequence of Fig. 13, plotted as a function of time in units of wingbeat periods

despite the fact that the wing loading is quite low. The phase-shifted time series shows how adjustments in position can be produced by cycle-to-cycle variation in upstroke function.

References

Adrian RJ (1991) Particle-imaging techniques for experimental fluid mechanics. Ann Rev Fluid Mech 23:261–304

Anderson JD (1984) Fundamentals of aerodynamics. McGraw-Hill, New York

Fincham AM, Spedding GR (1997) Low-cost, high resolution DPIV for measurement of turbulent fluid flow. Exp Fluids 23:449–462

Kokshaysky NV (1979) Tracing the wake of a flying bird. Nature 279:146–148

Lighthill MJ (1975) Mathematical biofluiddynamics. SIAM Press, Philadelphia, pp 151–178

Moreau RE (1972) The Palaearctic–African bird migration systems. Academic, London

Norberg UM (1990) Vertebrate flight. Springer, Berlin

Pennycuick CJ (1975) Mechanics of flight. In: Farmer DS, King JR, Parkes C (eds) Avian biology, vol 5. Academic, London, pp 1–75

Pennycuick CJ (1989) Bird flight performance: a practical calculation manual. Oxford University Press, Oxford

Pennycuick CJ, Alerstam T, Hedenström A (1997) A new low-turbulence wind tunnel for bird flight experiments at Lund University, Sweden. J Exp Biol 200:1441–1449

Prandtl L, Tietjens OG (1934) Applied hydro- and aeromechanics. Dover, New York

Raffel M, Willert C, Kompenhans J (1998) Particle image velocimetry: a practical guide. Springer, Berlin

Rayner JMV (1979a) A vortex theory of animal flight. II. The forward flight of birds. J Fluid Mech 91:731–763

Rayner JMV (1979b) A new approach to animal flight mechanics. J Exp Biol 80:17–54

Rayner JMV, Jones G, Thomas A (1986) Vortex flow visualizations reveal change in upstroke function with flight speed in bats. Nature 321:162–164

Spedding GR (1986) The wake of a jackdaw (*Corvus monedula*) in slow flight. J Exp Biol 125:287–307

Spedding GR (1987a) The wake of a kestrel (*Falco tinnunculus*) in gliding flight. J Exp Biol 127:45–57

Spedding GR (1987b) The wake of a kestrel (*Falco tinnunculus*) in flapping flight. J Exp Biol 127:59–78

Spedding GR (1992) The aerodynamics of flight. In: Alexander R McN (ed). Advances in comparative physiology. The mechanics of animal locomotion. Springer, Berlin, pp 51–111

Spedding GR, Rayner JMV, Pennycuick CJ (1984) Momentum and energy in the wake of a pigeon (*Columba livia*) in slow flight. J Exp Biol 111:81–102

Spedding GR, Rignot EJM (1993) Performance analysis and application of grid interpolation techniques for fluid flows. Exp Fluids 15:417–430

Westerweel J (1993) Digital particle image velocimetry. Delft University Press, Delft